Version of Record: https://www.sciencedirect.com/science/article/pii/S016943322100564X
Manuscript_146f5aa8fe914470507eb283293231b3

Surface structures of magnetostrictive $D0_3$-Fe_3Ga(001)

Ricardo Ruvalcaba[1], Joseph P. Corbett[2*], Andrada-Oana Mandru[3], Noboru Takeuchi[1], Arthur R. Smith[4], Jonathan Guerrero-Sanchez[1]

[1]*Centro de Nanociencias y Nanotecnología, Universidad Nacional Autónoma de México, Ensenada, BC 22860, Mex.*
[2]*Department of Physics, the Ohio State University, Columbus, OH 43210, USA*
[3]*Empa, Swiss Federal Laboratories for Materials Science and Technology, Dübendorf CH-8600, Switzerland*
[4]*Nanoscale and Quantum Phenomena Institute—Department of Physics and Astronomy, Ohio University, Athens, OH 45701, United States of America*
[*]*corbett.123@osu.edu, guerrero@cnyn.unam.mx*

Abstract

First-principles total energy calculations and scanning tunneling microscopy experiments were performed to study the surface reconstruction of the magnetostrictive Fe_3Ga alloy. The inverse magnetostrictive behavior was evaluated in the bulk by compressing and stretching its lattice parameter, showing an increase in magnetic moments as strain increases. Surface analysis demonstrates two thermodynamically stable surfaces, the (1×1) and (3×1). The (1×1) is an ideal FeGa terminated surface, whereas the (3×1) is also FeGa terminated but it has a first-layer Fe atom substituted by a Ga atom every three unit-cells, forming a row-like surface structure. Tersoff–Hamann scanning tunneling microscopy simulations were obtained and compared with experimental results. We found good agreement between theory and experiment, in which the distance between rows is ~12.3 Å. Theoretical findings suggest that the substrate-induced strain may increase the stability of the (3×1) reconstruction. Analysis of the magnetic moments in the reconstructions showed that their behavior is affected by a surface effect, as well as by the inverse magnetostriction of the structure. A good understanding of the surface reconstructions of FeGa is an important step towards further improvements in magnetic storage devices and sensors.

Keywords: Ga/Fe atomic exchange, strain, thermodynamic stability, magnetic moment enhancement.

1. Introduction

Although magnetism can be considered as a well-studied phenomenon, there is current

important research on several magnetic features, such as topological magnetism [1], magnetic fluids, magneto electrochemistry, and characteristics of magnetic materials [2]. The ability to change the magnetization when strain is applied, and when it is released, allows one to create wireless, passive sensors that can detect applied force [3], stress [4], and even strain [5], all of which can then be applied in technological devices. Particularly in the medical field, inverse magnetostrictive sensors have been used for measuring the load on biomedical implants and devices and creating scaffolds for bone-tissue engineering [6,7], as well as monitoring the strain on a bone plate [8], the degradation of artificial bones in-vitro [9], and the tensile force on sutured wound sites [10], to mention some examples. Also, sensors for many different chemicals can be created by using electrodeposition to produce coatings of magnetostrictive materials. Some of the chemicals that these sensors can successfully detect are carbon dioxide [11], ammonia [12], glucose [13], ricin [14], avidin [15], and staphylococcal enterotoxin B [16]. Additionally, because of its mechanical response to a magnetic signal, magnetostrictive materials may also be used as magnetic and magneto-optic actuators [17,18]. The inverse magnetostriction effect in some materials can be used to develop advanced ultra-thin spintronic nanodevices with customized electronic and magnetic properties by local strain engineering and ultra-low-power magnetoelectric memory devices [19,20]. Finally, a changing magnetic field can be used in conjunction with a magnetostrictive material to produce vibrations. Such vibrators have already been proposed [21,22], and they can be used in a wide range of applications: anything from machining hard materials [23], structural vibration control [24,25], to making a motor [26,27].

Among the magnetic alloys, Galfenol ($Fe_{100-x}Ga_x$) has more desirable mechanical properties than Terfenol-D ($Tb_xDy_{1-x}Fe_2$), the most common magnetostrictive material used in engineering [28]. Galfenol has sufficient ductility for sensor and actuator applications [29], and

films made out of it may be used to develop magnetic sensors for high-temperature applications with superior performance to that of the current ones [30].

In the past several years, there have been many studies regarding Galfenol's magnetic and mechanical properties [31,32,33]. Particularly, Mandru *et al*. [34] investigated the growth and magnetic properties of varying-composition FeGa when deposited onto non-magnetic and antiferromagnetic substrates. Substrate-induced perpendicular magnetic anisotropy was present in the samples grown onto antiferromagnetic substrates, similar to the case of FeGa grown on ZnSe/GaAs(001) [35]. In addition, row-like surface structures were observed by scanning tunneling microscopy (STM) for high Ga contents.

Out of all the samples investigated in Ref. [34], we focus on the one containing 23.6 ± 2.4 at.% Ga and prepared at 320 °C. Given the growth temperature and also the Ga content and its uncertainty, this sample is in the compositional range where either only the ordered $D0_3$ phase or a mixture of mostly $D0_3$ and a disordered A2 phase can occur [36]. Nevertheless, it has been reported that $D0_3$ and another ordered phase, B2, may coexist, depending on the thermodynamic history of the sample [37]. An example of this is the work by Eddrief et al. [38], where a B2 phase was formed at ~180 °C due to Ga-Ga pairing along the [001] direction. The reported B2-like structure is similar to $D0_3$, differing only on the position of the Fe and Ga atoms on the (002) plane [39]. However, considering their energetics [39], we choose the $D0_3$ as the main candidate to host the observed row structures.

In this paper, we simulate the $D0_3$-Fe_3Ga by spin-polarized density functional theory (DFT) and explore the inverse magnetostriction by straining the lattice and observing the impact on the magnetic moment carried by Fe and Ga. Additionally, we build upon previous work to

describe the surface structures responsible for the row-like patterns on the $D0_3$-Fe_3Ga(001) by means of thermodynamic stability analysis and STM experiments. Our results indicate two stable surface structures: an ideal (1×1) FeGa terminated surface and a (3×1) FeGa terminated reconstruction with an atomic Ga/Fe exchange (a Ga atom takes an Fe atom's place on the surface) every three unit-cells, leading to the formation of Ga channels, as evidenced in the calculated STM images, which agrees very well with the experimental STM images. The magnetic moments of the atoms of both surfaces are discussed taking into consideration both the surface and the inverse magnetostrictive effects. The rest of the paper is organized as follows: In section 2 we describe the methodology, in section 3 we present and discuss the results, and finally, in section 4 we summarize and present some perspectives.

2. Materials and methods

Spin-polarized calculations were performed using the Plane-Wave Self-Consistent Field code as implemented in the Quantum ESPRESSO package [40]. The exchange-correlation energy was calculated based on the Generalized Gradient Approximation (GGA) by employing the Perdew–Burke–Ernzerhof (PBE) parametrization [41]. Ultrasoft scalar-relativistic pseudopotentials were used in all calculations [42]. DFT+U calculations were performed on the bulk structure since the Fe atoms typically have strongly correlated electronic states due to their localized d orbitals. However, this its use was discarded because it does not correctly describe the physical properties of the system. We present more details about this in section S.1 of the supplementary section. The kinetic energy cut-off for wavefunctions and charge density were set to 45 and 360 Ry, respectively. The atomic relaxations and self-consistent calculations were performed using Brillouin-zone Monkhorst-Pack Γ-centered grids of (10×10×10) k-points for the bulk, and (10×10×1), (5×10×1), and (3×10×1) k-points for the (1×1), (2×1) and (3×1) surfaces,

respectively [43]. Methfessel-Paxton broadening with a smearing width of 1×10^{-2} Ry was used [44]. The bulk structure was energetically and structurally optimized and the lattice parameters used for the rest of the paper are *a, c* = 4.09, 5.81 Å for the $D0_3$ phase, which are in excellent agreement with the reported values *a, c* = 4.10, 5.79 Å [39, 45]. The improved tetrahedron method as implemented by Blöchl et al. [46] was used to calculate the total and projected Density of States (DOS). The magnetic moment of each atom was analyzed for the $D0_3$ phase at strains ranging from -1% to +3% both, iso- and anisotropically. The Surface Formation Energy (SFE) formalism adapted from Qian, Martin, and Chadi was used to determine the most stable surface reconstruction [47]. The supercell method was employed to simulate the surface reconstructions, with a thickness of 7 atomic layers per surface (~0.87 nm) and leaving empty spaces of ~11 Å to separate the surfaces in order to avoid interaction with their equivalent surfaces generated due to the imposed periodicity. Finally, STM images as implemented by Tersoff-Hamann were obtained for the most stable surfaces at 4 Å with a bias voltage of +2.0 V [48], as utilized in the experiments presented in Ref. [34].

The 48 ± 4 nm-thick sample was prepared at 320 °C in a custom-built molecular beam epitaxy system with a base pressure of 1.0×10^{-10} Torr. Sample composition was determined *ex-situ* by Rutherford backscattering spectrometry and crystalline properties were determined by X-ray diffraction and reflection high-energy electron diffraction. Further details regarding growth characterization can be found in Ref. [34]. The sample was transferred *in-situ* to a second ultra-high vacuum chamber housing a custom-built room temperature scanning tunneling microscope. Imaging was done with etched tungsten tips that had been previously annealed in vacuum to remove oxide.

3. Results and Discussions

3.1. Magnetic Properties of the Fe_3Ga Bulk Structure

Bulk Fe_3Ga was studied in the $D0_3$ phase, which has a face-centered tetragonal (FCT) structure [39], see Fig. 1(a). Different magnetic configurations of the FeGa alloy were structurally relaxed and the electronic properties of the ferromagnetic structure (the most stable one) were also analyzed. Note that since these results are not the main focus of this study, they are presented in section S.2 of the supplementary section.

We now proceed to analyze the inverse magnetostrictive behavior of the $D0_3$ structure [see Fig. 1(b)] considering that in Ref. [34] FeGa is grown on MnN substrates. The $D0_3$ structure was strained up to 3% and the impact on the magnetic moments was calculated. For the sake of completeness, we also compressed the system by 1%. Isotropic and anisotropic (in-plane) strains were analyzed. The magnetic moments increase linearly as a function of the strain within the region examined for both cases. This smooth change of the magnetic moments has been previously reported on Fe_3Ga [37], the very similar Fe_3Ni [49,50], other Fe-alloys such as Fe_3InN_4 [51], and Fe_4C [52]. Interestingly, Fe(1)'s magnetic moment is always greater than Fe(2)'s. This phenomenon is associated with the weak Fe-Ga hybridization in the Fe(2) atoms (as shown in Fig. S2(b) in Supplementary information). The inverse magnetostrictive behavior of Fe_3Ga alloys can be attributed to the presence of nonbinding Fe d-states around the Fermi level. A more detailed explanation of this phenomenon has been given in Ref. [53].

The row-like structures experimentally found on the sample deposited onto antiferromagnetic MnN in Ref. [34] are not caused by the inverse magnetostriction of the Fe_3Ga alloy nor the lattice mismatch induced by the substrate. They are more likely to be a series of surface reconstructions. The assessment of this idea is discussed in the following sections.

3.2. Stability of the Fe_3Ga(001) Surfaces

Different possible reconstruction models are considered in our analysis. They include not only the Fe-, and ideal FeGa-terminated surfaces, but also structures with ad-atoms, and with Fe/Ga substitutions. Since we are dealing with different numbers of atoms, the total energies of these systems are not comparable. Therefore, we use the surface formation energy (SFE) to study their relative stability [47,54]. To apply this formalism, we must consider thermal equilibrium between vacuum (reservoir), surface, and bulk. So each change in energy due to the addition or removal of atoms is registered by their corresponding chemical potentials. For condensed phases, chemical potentials are defined as the total energy per atom of their most stable bulk structure [47]. The expression for the SFE in the proposed systems is:

$$SFE = \frac{1}{2A}\left[E_{slab} - \mu_{bulk}\left(\frac{1}{6}n_{Fe} + \frac{1}{2}n_{Ga}\right) - \Delta\mu\left(\frac{1}{6}n_{Fe} - \frac{1}{2}n_{Ga}\right)\right] \quad (1)$$

where A is the surface area, E_{slab} is the final energy of each surface, n_{Fe} and n_{Ga} are the numbers of atoms of each element present in the surface, and μ_{Fe}, μ_{Ga}, and μ_{bulk} are the chemical potentials of the Fe, Ga, and $D0_3$-Fe_3Ga bulk structures, respectively. The SFE was plotted from Ga-rich ($-\Delta H_f \leq \Delta\mu \leq 0$) to Fe-rich conditions ($0 \leq \Delta\mu \leq \Delta H_f$), where ΔH_f is the Fe_3Ga formation enthalpy, defined as $\Delta H_f = 3\mu_{Fe} + \mu_{Ga} - \mu_{bulk}$, which defines the allowed growth limits. The formation enthalpy was found to be 0.188 eV/Fe_3Ga unit ($D0_3$ phase), which is in agreement with the reported value of 0.416 ± 0.328 eV/Fe_3Ga unit [55]. A positive value under this definition means that the $D0_3$ phase is more stable than its constituents (Fe and Ga chemical potentials), otherwise if negative.

Figure 2 illustrates the supercells the proposed surface reconstructions are based on. They are labelled as follows: (reconstruction periodicity).(metal added).(position of

adsorption/substitution). The notation a_x and s_x (x=1,2,3) stands for adsorption and substitution positions on the surfaces, respectively [see Figs 2(a,b)]. Hence, reconstructions A.Fe.a_1 and A.Fe.a_2 have (2×1) periodicities with an Fe atom adsorbed in positions a_1 and a_2, respectively (Fig. S3 in Supplementary information). The same goes for A.Ga.a_1 and A.Ga.a_2 but with Ga atoms. Reconstruction A.Ga.s_1 has a (2×1) periodicity with a Ga atom substituting the Fe atom in position s_1. Similarly, reconstructions B.Fe.a_3 and B.Ga.a_3 have (3×1) periodicities with Fe/Ga atoms adsorbed in position a_3, respectively. Finally, reconstructions B.Fe.s_2 and B.Ga.s_3 have (3×1) periodicities with Fe/Ga atoms substituted in positions s_2 and s_3, respectively, see Fig. S3 in the supplementary section. Notice that adsorption positions can be filled with both metals whilst substitutions only with one. This happens because one atom replacing another one of the same element leaves the surface unchanged. Inversion symmetry was kept in every cell, therefore having two equivalent surfaces.

Results of the stability analysis are plotted in Fig. 3, where the lowest energy values are related to the most stable surfaces. There is a clear trend in the data. For non-strained lattice parameters [Fig. 3(a)], the ideal Fe-terminated surface [A in Fig. 2(a)] is always less stable than the FeGa-terminated surface (B in Fig. 2(b)). Moreover, if Fe is added (either by substituting or adsorbing it) to any of the surfaces they become less favorable, and the opposite happens by adding Ga. Neither A nor any of its modified structures with (2×1) periodicities are stable for any chemical potential. On the other hand, the stable surfaces are the ideal FeGa-terminated (B) with a (1×1) symmetry for Fe rich conditions and the (3×1) reconstruction induced in the FeGa-terminated surface by making it Ga rich. In this case, an Fe atom of the first layer has been exchanged by a Ga atom, which leads to a stable structure [B.Ga.s_3 reconstruction in Fig. 2(c)]. This surface is stable from Ga intermediate to Ga rich conditions. The stability range of this

reconstruction was expected since this surface has a deficit of Fe in the first layer. Note that Fe adsorbed on the Fe-terminated surface is the least stable reconstruction. In this case, a (2×1) unit cell was used. However, if we start with the Fe layer in a larger unit cell, adding Fe ad-atoms would be unfavorable as adding Fe atoms increases the formation energy. In the case of a Ga replacement, this would improve the stability, but so little Ga is being added that it would be approximately equal to the ideal Fe SFE. Furthermore, for more densely Ga-substituted Fe surfaces, the SFE is still significantly higher than the ideal and substituted FeGa terminations. Therefore, we focus on the FeGa termination and the atomic substitutions that could give rise to the observed row-structure. Fe adsorbed on the FeGa terminated surface diminishes its stability. Fe substitution on the FeGa-terminated surface is also unstable. Note that the structures stabilize as they increase their Ga content. It is therefore expected that Ga layers could be engineered in this system. Similar results reporting stable Ga layers have recently appeared in the literature [56].

We next analyze the effect of strain on the stability of the surface [Fig. 3(b)]. Generally speaking, in an experimental growth procedure, the film may experience an elongation or contraction of its lattice parameter until a critical thickness in order to match the one imposed by the substrate. Here we simulate a maximum strain of 3% induced to the $D0_3$-Fe_3Ga surfaces, and analyze how it affects the stability of the favored models. Such difference in lattice mismatch is small enough to assure epitaxial growth with a minimum quantity of defects at the interface. Induced strain (~3%) reduces the growth limit imposed by the formation enthalpy, from 0.188 to 0.156 eV/Fe_3Ga unit. Stable models were also fully optimized (structurally and energetically without any restriction) with the new lattice parameter. Note that the (1×1) FeGa terminated surface experiences a decrease in stability, being achievable just for very Fe-rich conditions. On

the other hand, the (3×1) B.Ga.S_3 structure gains stability and is favored for almost all growth conditions, see Fig. 3(b). These results indicate that the extra Ga atoms on the (3×1) surface may help to stabilize the (3×1) reconstruction in the ultra-thin film limit. In the experiment, whether the surface of the film has a strained or an optimal lattice parameter depends on its thickness. If the film is above a certain critical thickness, the lattice parameter at the superficial layers will not be strained and will have its optimal value. In any case, for both scenarios the (3×1) reconstruction is the most stable for the conditions used in the experiment (Ga-rich).

3.3 Scanning tunneling microscopy analysis: DFT and experimental data

Since one of the goals of this work is to explain the row-structure appearing in the $D0_3$-Fe_3Ga thin films, we proceed to compare the theoretical Tersoff-Hamann STM (TH-STM) images with the experimental results. In the Fe-Ga phase diagram, films containing 15 to 23 at.% Ga grow in a mixed phase of disordered A_2 and ordered tetragonal $D0_3$. Above 23 at.% Ga, phases of $D0_3$ and potentially B2 coexist [57]. The samples were prepared under Ga concentrations of ~23 at.% Ga, which favors predominantly the $D0_3$ phase as explained before. From the bulk crystalline phase diagram, accessing the different phases depends critically on the formation temperatures and quenching rates [57,58]. For example, B_2-like clusters were observed within A_2 in thin films, at concentration of ~15 at.% Ga. [38] While these formation windows can be similar for thin-film growth, it is worth reminding that in the theoretical phase diagram, the $D0_3$ is the stable phase for our considered case of 23.6 at.% Ga [58].

As mentioned before, STM investigations revealed row-structures on FeGa thin films with ~23 at.% Ga concentration [34], similar to the rows found on the L10-MnGa/ $\eta_{\perp}$-Mn_3N_2 bilayer [59], or on Mn_3N_2(010) [60]. A well-ordered (3×1) structure with a row spacing of 12.8 ±

0.5 Å (narrow rows), and a dislocated (4.5×1) structure with a row spacing of 18.6 ± 0.5 Å (wide rows) were observed, see Fig. 4a. Through the use of DFT and TH-STM images, we are able to untangle the makeup of these previously-observed row structures.

Since the A_2 structure is α-Fe with random Ga substitutions, it would seem unlikely that an ordered surface structure would emerge. If this row-structure does arise from an A_2 phase, it would be a (6×1) and (9×1) surface structure for the narrow and wide rows respectively. This would be a scenario with larger surface unit cells and many equivalent unoccupied substitution sites between the rows, leading one to suspect this as an unlikely scenario given the high concentration of Ga and the well-ordered surface. Therefore, we investigate the $D0_3$ phase as the candidate to host the row-structure.

Theoretical TH-STM images of the two lowest energy (3×1) and (1×1) structures are computed [Figs. 4(c-d)] and compared to the experimental STM images [Figs. 4(a-b)]. The (3×1) reconstruction produces a pronounced row-structure. Fast Fourier Transforms (FFT) of the experimental and theoretical STM images are shown in Figs. 4(e-g). A line of dense k-points corresponds to the (3×1) row-structure, as indicated by the green arrows in Fig. 4(e,f). The FFT of the (3×1) TH-STM image has additional weaker k-points in a square array (see blue arrow) corresponding to the underlying FeGa surface structure while the FFT of the experimental STM image lacks the additional weaker k-points. However, this is to be expected because to first order, the STM reciprocal space points with the smallest k-vector magnitudes usually dominate the image. A similar behavior has been observed in Mn_3N_2(010) surfaces, where row-like reconstructions are easily seen, but their underlying atomic resolution is more difficult [60]. Further STM measurements are necessary to image the row-patterns atomic arrangement seen in the theoretical STM image [Fig. 4(c)]. The FFT of the ideally terminated (1×1) FeGa surface

shows a square array of 4 k-points indicated by the blue arrow in Fig. 4(g). Overall, good agreement is achieved between the experimental STM and TH-STM images, enabling us to propose the (3×1) row-structure as a Ga-substituted FeGa-terminated surface.

From the previous work [34], the XRD measurements showed a tetragonally distorted cubic cell (~2%) with an *in-plane* lattice parameter of 4.045 ± 0.02 Å, which corresponds to a (3×1) spacing of 12.13 ± 0.06 Å [34]. While the measured surface lattice parameter is larger than that expected from XRD, however to within error, the STM row spacing measurement is in agreement with the XRD estimate of the row-spacing. The XRD is an average measurement of the lattice from the bulk to the film, while the STM measurement is local to the surface. The presence of the dislocated wide rows often coexists with the narrow rows (see Fig. 4(a) marked by N W N), which could account for the slightly larger (to within error) row spacing. Furthermore, from the STM measurement we do not have evidence to suggest any strain present on the surface lattice, while we know the bulk of the lattice is slightly distorted. The TH-STM images are calculated from the ideal unstrained case and compared to the experimental STM images. We know from SFE calculations that straining the lattice improves the favorability of the Ga substituted (3×1) lattice which leads us to believe the tetragonal distortion would not change the (3×1) assignment.

Further experimental and theoretical investigations are needed to untangle the details of the (4.5×1) row-structure. We suspect this is a Ga-substitution given the SFE trend and that wide rows can coexist within narrow rows as seen in Fig. 4(a). In the event that a $D0_3$ phase-based surface does not satisfactorily explain the (4.5×1) row-structure or the non-periodic region shown in Fig. 4(a), it is hypothesized that the B2-like phase could be present at the surface producing the previously mentioned structures. There are additional regions without periodic

structure, as indicated by the dotted light blue borders, which coexist with the (3×1) structure. These regions without periodic structure could be nano-crystalline inclusions of A2 [34], or the ideal FeGa-terminated layer. Further work should be done to increase the resolution of the row-structures and regions without periodic structure to pin down additional details that cannot be achieved from this analysis. While we have evidence to believe the rows are hosted by the $D0_3$-Fe_3Ga crystal, the SFE calculations follow in suit with this assumption, it nevertheless begs for additional resolution as also observed in the Mn_3N_2 system [60].

3.4 Magnetic Moments Analysis

The Fe_3Ga (001) surfaces present a ferromagnetic behavior with its main contributions coming from Fe atoms. Ga atoms make a small contribution but in the opposite direction. Figure 5 shows the magnetic moment analysis per surface layer, from the surface to the bulk layers, for the non-strained (optimized), and strained lattice cases (as a reminder, the maximum induced strain is of the order of 3%). The values of the bulk magnetic moments for Fe(1) and Fe(2) atoms are also included for comparison, as horizontal solid (optimized structure) and dashed (strained structure) lines, respectively. In the latter structure, the strain is applied to each atomic layer with the same value.

Figure 5(a) shows that the (1×1) surface experiences an increase in the superficial Fe(1) atom's magnetic moment due to the formation of the surface. The absence of some of the neighboring atoms and subsequent relaxation of the surface increases its magnetic moment by ~0.5 μ_B/atom in comparison to the bulk. The Fe(2) atoms in the second (Fe-only) layer experience a similar surface effect, but reducing their magnetic moment by ~0.05 μ_B/atom in comparison to the bulk. This surface phenomenon affects the layers that are closer to the surface,

and it is negligible after the second layer. The farther the layers are from the surface, the more they behave as in the bulk structure. The strained surface shows basically the same behavior, with the difference that the inverse magnetostrictive effect of the Fe_3Ga causes the overall magnetic moment to increase by ~0.02 μ_B/atom and ~0.04 μ_B/atom in the Fe(1) and Fe(2) bulk layers, respectively.

Figure 5(b) shows the behavior of the Fe magnetic moments for the (3×1) reconstruction . Here, three effects modify the magnetic behavior of the first layer: the previously mentioned surface and inverse magnetostrictive effects, and the Fe-for-Ga substitution effect. The latter is the reason why this structure is the most stable one, according to the analysis performed in Section 3.2. Interestingly, the incorporated Ga atom on position s_3 has a magnetic moment with a smaller magnitude (-0.09 μ_B) than the other Ga atoms on the surface layer (-0.23 μ_B). This difference in the value of the surface Ga magnetic moments may be due to hybridization with the neighboring Fe atoms, and to the interaction with the neighboring Ga atoms of the first layer, which shows an increase in its magnetic moment magnitude (-0.28 μ_B). For clarification, see Fig. 2(c) (B.Ga.s_3 model) and Fig. S4 in supplementary information. Again, note that the Fe(2) atoms at the strained surface layer have a larger magnetic moment in comparison to the ones of the non-strained (optimized) surface due to the inverse magnetostriction present in the structure. The surface phenomenon vanishes on the third layer and the magnetic moments resemble those of the bulk. Similar behavior is seen for deeper layers. The increase in magnetic moments due to strain becomes more apparent when getting farther away from the surface and closer to the bulk. In this reconstruction, the magnetic moments increase by ~0.04, and ~0.08 μ_B/Fe atom in the Fe(1) and Fe(2) bulk atoms, respectively. Finally, it is shown that the magnetic moments of the bulk Fe(2) layers with strained lattice parameters are ~0.1 μ_B different from the strained-bulk values

calculated in section 3.1. Here we have presented a comprehensive analysis of the substrate-induced strain in the stable surfaces. However, the effect of the interaction between the film and substrate atoms at the interface needs to be untangled to have the full knowledge of the change in magnetic properties due to different substrates, as reported in Ref. [34].

At the surface, the crystal's translational symmetry is broken, which intuitively results in an alteration of the material properties within that region. This surface effect has been observed experimentally on magnetic materials such as Co [61] or ferrite [62] nanoparticles. The surface effect may result from a combination of various factors, being the most relevant ones: the symmetry breaking of the crystal structure, dangling bonds, surface strain, or even different chemical and physical structures of internal and surface parts of the structure [62]. However, considering that the $D0_3$-Fe_3Ga is ferromagnetic and the atomic spins' direction were fixed in the calculation, the surface effect present on both surfaces is probably caused due to an e_g orbital reconstruction (similar to the one observed in manganites [63,64]) and the enhancement of the magnetic anisotropy which results from surface anisotropy (particularly in the B.Ga.S_3 model).

In Ref. [34], the average magnetic moment for the sample with 23.6 at.% Ga [measured by vibrating sample magnetometry (VSM) at room-temperature] was found to be 1.83 +/- 0.23 μ_B/Fe atom (red solid line in Fig. 5). This value is slightly lower than the values found here. However, this is to be expected considering that the VSM measurements provide an average value for the whole film, which can potentially include: i) much lower magnetic moments given by the material in the first several nm from the interface with MnN, or ii) lower magnetic moments from other areas (not sampled by STM) that may not have an ordered structure.

4. Conclusions

This paper presented *ab initio* calculations together with experimental STM measurements to study the $Fe_3Ga(001)$ surfaces. The magnetic moment behavior of the bulk $D0_3$ phase was studied when expanding the unit cell isotropically and anisotropically (in-plane), and it was associated with a weak Fe-Ga hybridization on the Fe layers. An FeGa-terminated (1×1) surface and a row-like (3×1) FeGa terminated surface, with a first-layer Fe exchanged by Ga atom each three unit cells, are the thermodynamically stable structures. Theoretical and experimental STM images were compared and found to be in good agreement. Theoretical findings suggest that when strain is induced within the stable surfaces, the (3×1) reconstruction turns to be the only favored structure, demonstrating that extra Ga atoms may help to stabilize the rows. A strong surface effect was observed in the magnetic moments, being prominent for the first two layers and vanishing for deeper layers. Our study is a step towards the understanding of the magnetostrictive Fe_3Ga atomic reconstructions. The tunable magnetic properties of this material make it a candidate to be used as part of magnetic heterojunctions with potential applications in spintronics devices.

Acknowledgments

We thank DGAPA-UNAM projects IN101019 and IA100920 and CONACYT grants A1-S-9070 for partial financial support. Experimental part of this research supported by the US Department of Energy, Office of Basic Energy Sciences, Division of Materials Sciences and Engineering under Award No. DE-FG02-06ER46317. Calculations were performed in the DGTIC-UNAM supercomputing center project LANCAD-UNAM-DGTIC-368. The authors thankfully acknowledge the computer resources, technical expertise and support provided by the *Laboratorio Nacional de Supercómputo del Sureste de México*, CONACYT member of the

network of national laboratories. JGS acknowledges THUBAT KAAL IPICYT supercomputing center for computational resources. The authors would like to thank E. Murillo, and A. Rodriguez Guerrero for technical assistance and useful discussions. Image analysis was performed by Gwyddion software package [65].

References

[1] M.-G. Han, J.A. Garlow, Y. Liu, H. Zhang, J. Li, D. DiMarzio, M.W. Knight, C. Petrovic, D. Jariwala, Y. Zhu, Topological Magnetic-Spin Textures in Two-Dimensional van der Waals $Cr_2Ge_2Te_6$, Nano Lett. 19 (2019) 7859–7865. https://doi.org/10.1021/acs.nanolett.9b02849.

[2] J. M. D. Coey, Magnetism and Magnetic Materials, Cambridge University Press, Cambridge, 2010, pp. 542–565.

[3] B.D. Pereles, A.J. DeRouin, K. Ghee Ong, A Wireless, Passive Magnetoelastic Force–Mapping System for Biomedical Applications, Journal of Biomechanical Engineering. 136 (2014) 011010. https://doi.org/10.1115/1.4025880.

[4] D. Kouzoudis, C.A. Grimes, The frequency response of magnetoelastic sensors to stress and atmospheric pressure, Smart Mater. Struct. 9 (2000) 885–889. https://doi.org/10.1088/0964-1726/9/6/320.

[5] N.P. Oess, B. Weisse, B.J. Nelson, Magnetoelastic Strain Sensor for Optimized Assessment of Bone Fracture Fixation, IEEE Sensors J. 9 (2009) 961–968. https://doi.org/10.1109/JSEN.2009.2025575.

[6] B.D. Pereles, A.J. DeRouin, K. Ghee Ong, A Wireless, Passive Magnetoelastic Force–Mapping System for Biomedical Applications, Journal of Biomechanical Engineering. 136 (2014) 011010. https://doi.org/10.1115/1.4025880.

[7] M.M. Fernandes, D.M. Correia, C. Ribeiro, N. Castro, V. Correia, S. Lanceros-Mendez, Bioinspired Three-Dimensional Magnetoactive Scaffolds for Bone Tissue Engineering, ACS Appl. Mater. Interfaces. 11 (2019) 45265–45275. https://doi.org/10.1021/acsami.9b14001.

[8] Yisong Tan, Jiale Hu, Limin Ren, Jianhua Zhu, Jiaqi Yang, Di Liu, A Passive and Wireless Sensor for Bone Plate Strain Monitoring, Sensors. 17 (2017) 2635. https://doi.org/10.3390/s17112635.

[9] K. Yu, L. Ren, Y. Tan, J. Wang, Wireless Magnetoelasticity-Based Sensor for Monitoring the Degradation Behavior of Polylactic Acid Artificial Bone In Vitro, Applied Sciences. 9 (2019) 739. https://doi.org/10.3390/app9040739.

[10] A. DeRouin, N. Pacella, C. Zhao, K.-N. An, K.G. Ong, A Wireless Sensor for Real-Time Monitoring of Tensile Force on Sutured Wound Sites, IEEE Trans. Biomed. Eng. 63 (2016) 1665–1671. https://doi.org/10.1109/TBME.2015.2470248.

[11] Q.Y. Cai, A. Cammers-Goodwin, C.A. Grimes, A wireless, remote query magnetoelastic CO2 sensor, J. Environ. Monitor. 2 (2000) 556–560. https://doi.org/10.1039/b004929h.

[12] Q.Y. Cai, M.K. Jain, C.A. Grimes, A wireless, remote query ammonia sensor, Sensors and Actuators B: Chemical. 77 (2001) 614–619. https://doi.org/10.1016/S0925-4005(01)00766-3.

[13] K. Ong, M. Paulose, M. Jain, D. Gong, O. Varghese, C. Mungle, C. Grimes, Magnetism-Based Remote Query Glucose Sensors, Sensors. 1 (2001) 138–147. https://doi.org/10.3390/s10500138.

[14] C. Ruan, K.O. Varghese, C.A. Grimes, K. Zeng, X. Yang, N. Mukherjee, K.G. Ong, A Magnetoelastic Ricin Immunosensor, Sen Lett. 2 (2004) 138–144. https://doi.org/10.1166/sl.2004.041.

[15] C. Ruan, K. Zeng, O.K. Varghese, C.A. Grimes, A magnetoelastic bioaffinity-based sensor for avidin, Biosensors and Bioelectronics. 19 (2004) 1695–1701. https://doi.org/10.1016/j.bios.2004.01.005.

[16] C. Ruan, K. Zeng, O.K. Varghese, C.A. Grimes, A staphylococcal enterotoxin B magnetoelastic immunosensor, Biosensors and Bioelectronics. 20 (2004) 585–591. https://doi.org/10.1016/j.bios.2004.03.003.

[17] S. Mondal, M.A. Abeed, K. Dutta, A. De, S. Sahoo, A. Barman, S. Bandyopadhyay, Hybrid Magnetodynamical Modes in a Single Magnetostrictive Nanomagnet on a Piezoelectric Substrate Arising from Magnetoelastic Modulation of Precessional Dynamics, ACS Appl. Mater. Interfaces. 10 (2018) 43970–43977. https://doi.org/10.1021/acsami.8b19243.

[18] H.-J. Liu, L.-Y. Chen, Q. He, C.-W. Liang, Y.-Z. Chen, Y.-S. Chien, Y.-H. Hsieh, S.-J. Lin, E. Arenholz, C.-W. Luo, Y.-L. Chueh, Y.-C. Chen, Y.-H. Chu, Epitaxial Photostriction–Magnetostriction Coupled Self-Assembled Nanostructures, ACS Nano. 6 (2012) 6952–6959. https://doi.org/10.1021/nn301976p.

[19] Y. Ma, D. Hunt, K. Meng, T. Erickson, F. Yang, M.A. Barral, V. Ferrari, A.R. Smith, Local strain-dependent electronic structure and perpendicular magnetic anisotropy of a MnGaN 2D magnetic monolayer, Phys. Rev. Materials. 4 (2020) 064006. https://doi.org/10.1103/PhysRevMaterials.4.064006.

[20] Z. Xiao, R. Lo Conte, M. Goiriena-Goikoetxea, R.V. Chopdekar, C.-H.A. Lambert, X. Li, A.T. N'Diaye, P. Shafer, S. Tiwari, A. Barra, A. Chavez, K.P. Mohanchandra, G.P. Carman, K.L. Wang, S. Salahuddin, E. Arenholz, J. Bokor, R.N. Candler, Tunable Magnetoelastic Effects in Voltage-Controlled Exchange-Coupled Composite Multiferroic Microstructures, ACS Appl. Mater. Interfaces. 12 (2020) 6752–6760. https://doi.org/10.1021/acsami.9b20876.

[21] Washington, P.G. Magnetostrictive vibrator. U.S. Patent 1,882,397, Oct 10, 1932.

[22] T. Ueno, E. Summers, M. Wun-Fogle, T. Higuchi, Micro-magnetostrictive vibrator using iron–gallium alloy, Sensors and Actuators A: Physical. 148 (2008) 280–284. https://doi.org/10.1016/j.sna.2008.08.017.

[23] Balamuth, L. Magnetostrictive vibrator for high frequency machining of hard materials. U.S. Patent 3,471,724, Jul 10, 1969.

[24] S.-J. Moon, C.-W. Lim, B.-H. Kim, Y. Park, Structural vibration control using linear magnetostrictive actuators, Journal of Sound and Vibration. 302 (2007) 875–891. https://doi.org/10.1016/j.jsv.2006.12.023.

[25] F. Braghin, S. Cinquemani, F. Resta, A model of magnetostrictive actuators for active vibration control, Sensors and Actuators A: Physical. 165 (2011) 342–350. https://doi.org/10.1016/j.sna.2010.10.019.

[26] Abbot, F. Magnetostrictive vibration motor. U.S. Patent 3,470,402, Sep 30, 1969.

[27] F. Claeyssen, N. Lhermet, R. Le Letty, P. Bouchilloux, Actuators, transducers and motors based on giant magnetostrictive materials, Journal of Alloys and Compounds. 258 (1997) 61–73. https://doi.org/10.1016/S0925-8388(97)00070-4.

[28] A.E. Clark, Chapter 7 Magnetostrictive rare earth-Fe_2 compounds, in: Handbook of Ferromagnetic Materials, Elsevier, 1980: pp. 531–589. https://doi.org/10.1016/S1574-9304(05)80122-1.

[29] J.J. Park, S.-M. Na, G. Raghunath, A.B. Flatau, Stress-anneal-induced magnetic anisotropy in highly textured Fe-Ga and Fe-Al magnetostrictive strips for bending-mode vibrational energy harvesters, AIP Advances. 6 (2016) 056221. https://doi.org/10.1063/1.4944772.

[30] Z. Zhang, H. Wu, L. Sang, Y. Takahashi, J. Huang, L. Wang, M. Toda, I.M. Akita, Y. Koide, S. Koizumi, M. Liao, Enhancing Delta E Effect at High Temperatures of Galfenol/Ti/Single-Crystal Diamond Resonators for Magnetic Sensing, ACS Appl. Mater. Interfaces. 12 (2020) 23155–23164. https://doi.org/10.1021/acsami.0c06593.

[31] A. Clark, M. Wun-Fogle, J.B. Restorff, T.A. Lograsso, Magnetostrictive Properties of Galfenol Alloys Under Compressive Stress, Mater. Trans. 43 (2002) 881–886. https://doi.org/10.2320/matertrans.43.881.

[32] E.M. Summers, T.A. Lograsso, J.D. Snodgrass, J.C. Slaughter, Magnetic and mechanical properties of polycrystalline Galfenol, in: D.C. Lagoudas (Ed.), San Diego, CA, 2004: p. 448. https://doi.org/10.1117/12.539781.

[33] G. Petculescu, K.B. Hathaway, T.A. Lograsso, M. Wun-Fogle, A.E. Clark, Magnetic field dependence of galfenol elastic properties, Journal of Applied Physics. 97 (2005) 10M315. https://doi.org/10.1063/1.1855711.

[34] A.-O. Mandru, J.P. Corbett, A.L. Richard, J. Gallagher, K.-Y. Meng, D.C. Ingram, F. Yang, A.R. Smith, Magnetostrictive iron gallium thin films grown onto antiferromagnetic manganese nitride: Structure and magnetism, Appl. Phys. Lett. 109 (2016) 142402. https://doi.org/10.1063/1.4963761.

[35] M. Barturen, J. Milano, M. Vásquez-Mansilla, C. Helman, M.A. Barral, A.M. Llois, M. Eddrief, M. Marangolo, Large perpendicular magnetic anisotropy in magnetostrictive $Fe_{1-x}Ga_x$ thin films, Phys. Rev. B. 92 (2015) 054418. https://doi.org/10.1103/PhysRevB.92.054418.

[36] O. Ikeda, R. Kainuma, I. Ohnuma, K. Fukamichi, K. Ishida, Phase equilibria and stability of ordered b.c.c. phases in the Fe-rich portion of the Fe–Ga system, Journal of Alloys and Compounds. 347 (2002) 198–205. https://doi.org/10.1016/S0925-

[37] C. Paduani, C. Bormio-Nunes, Density functional theory study of Fe_3Ga, Journal of Applied Physics. 109 (2011) 033705. https://doi.org/10.1063/1.3525609.

[38] M. Eddrief, Y. Zheng, S. Hidki, B. Rache Salles, J. Milano, V.H. Etgens, M. Marangolo, Metastable tetragonal structure of $Fe_{100-x}Ga_x$ epitaxial thin films on ZnSe/GaAs(001) substrate, Phys. Rev. B. 84 (2011) 161410. https://doi.org/10.1103/PhysRevB.84.161410.

[39] R. Wu, Origin of large magnetostriction in FeGa alloys, J. Appl. Phys. 91 (2002) 7358. https://doi.org/10.1063/1.1450791.

[40] P. Giannozzi, S. Baroni, N. Bonini, M. Calandra, R. Car, C. Cavazzoni, D. Ceresoli, G.L. Chiarotti, M. Cococcioni, I. Dabo, A. Dal Corso, S. de Gironcoli, S. Fabris, G. Fratesi, R. Gebauer, U. Gerstmann, C. Gougoussis, A. Kokalj, M. Lazzeri, L. Martin-Samos, N. Marzari, F. Mauri, R. Mazzarello, S. Paolini, A. Pasquarello, L. Paulatto, C. Sbraccia, S. Scandolo, G. Sclauzero, A.P. Seitsonen, A. Smogunov, P. Umari, R.M. Wentzcovitch, QUANTUM ESPRESSO: a modular and open-source software project for quantum simulations of materials, J. Phys.: Condens. Matter. 21 (2009) 395502. https://doi.org/10.1088/0953-8984/21/39/395502.

[41] J.P. Perdew, K. Burke, M. Ernzerhof, Generalized Gradient Approximation Made Simple, Phys. Rev. Lett. 77 (1996) 3865–3868. https://doi.org/10.1103/PhysRevLett.77.3865.

[42] A.M. Rappe, K.M. Rabe, E. Kaxiras, J.D. Joannopoulos, Optimized pseudopotentials, Phys. Rev. B. 41 (1990) 1227–1230. https://doi.org/10.1103/PhysRevB.41.1227.

[43] H.J. Monkhorst, J.D. Pack, Special points for Brillouin-zone integrations, Phys. Rev. B. 13 (1976) 5188–5192. https://doi.org/10.1103/PhysRevB.13.5188.

[44] M. Methfessel, A.T. Paxton, High-precision sampling for Brillouin-zone integration in metals, Phys. Rev. B. 40 (1989) 3616–3621. https://doi.org/10.1103/PhysRevB.40.3616.

[45] X. Zhao, N. Mellors, S. Kilcoyne, D. Lord, N. Lupu, H. Chiriac, P.F. Henry, Neutron diffraction studies of magnetostrictive Fe–Ga alloy ribbons, Journal of Applied Physics. 103 (2008) 07B320. https://doi.org/10.1063/1.2837244.

[46] P.E. Blöchl, O. Jepsen, O.K. Andersen, Improved tetrahedron method for Brillouin-zone integrations, Phys. Rev. B. 49 (1994) 16223–16233. https://doi.org/10.1103/PhysRevB.49.16223.

[47] G.-X. Qian, R.M. Martin, D.J. Chadi, First-principles study of the atomic reconstructions and energies of Ga- and As- stabilized GaAs(100) surfaces, Phys. Rev. B. 38 (1988) 7649–7663. https://doi.org/10.1103/PhysRevB.38.7649.

[48] J. Tersoff, D.R. Hamann, Theory of the scanning tunneling microscope, Phys. Rev. B. 31 (1985) 805–813. https://doi.org/10.1103/PhysRevB.31.805.

[49] V.L. Moruzzi, High-spin and low-spin states in Invar and related alloys, Phys. Rev. B. 41 (1990) 6939–6946. https://doi.org/10.1103/PhysRevB.41.6939.

[50] J. Bohland Filho, C. A. Kuhnen, Electronic and Magnetic Structure of Ordered Fe-Ni Alloys. Brazilian Journal of Physics 23 (1993), 288–298

[51] P. Lukashev, W.R.L. Lambrecht, First-principles study of the structural and magnetic properties of iron indium nitride, Journal of Applied Physics. 97 (2005) 10D309. https://doi.org/10.1063/1.1847849.

[52] A.V. dos Santos, M.I. da Costa, C.A. Kuhnen, Electronic structure and magnetic properties of Fe_4C, Journal of Magnetism and Magnetic Materials. 166 (1997) 223–230. https://doi.org/10.1016/S0304-8853(96)00445-3.

8388(02)00791-0.

[53] Y. Zhang, R. Wu, Mechanism of Large Magnetostriction of Galfenol, IEEE Trans. Magn. 47 (2011) 4044–4049. https://doi.org/10.1109/TMAG.2011.2158202.

[54] A.-O. Mandru, J. Pak, A.R. Smith, J. Guerrero-Sanchez, N. Takeuchi, Interface formation for a ferromagnetic/antiferromagnetic bilayer system studied by scanning tunneling microscopy and first-principles theory, Phys. Rev. B. 91 (2015) 094433. https://doi.org/10.1103/PhysRevB.91.094433.

[55] $GaFe_3$ http://oqmd.org/materials/entry/18835 (accessed Aug 27, 2020).

[56] M.G. Moreno-Armenta, J.P. Corbett, R. Ponce-Perez, J. Guerrero-Sanchez, A DFT study on the austenitic Ni_2MnGa (001) surfaces, Journal of Alloys and Compounds. 836 (2020) 155447. https://doi.org/10.1016/j.jallcom.2020.155447.

[57] O. Goldbeck, IRON-Binary Phase Diagrams, Springer, Berlin, 1982, pp. 41.

[58] M.V. Matyunina, M.A. Zagrebin, V.V. Sokolovskiy, O.O. Pavlukhina, V.D. Buchelnikov, A.M. Balagurov, I.S. Golovin, Phase diagram of magnetostrictive Fe-Ga alloys: insights from theory and experiment, Phase Transitions. 92 (2019) 101–116. https://doi.org/10.1080/01411594.2018.1556268.

[59] J.P. Corbett, J. Guerrero-Sanchez, J.C. Gallagher, A.-O. Mandru, A.L. Richard, D.C. Ingram, F. Yang, N. Takeuchi, A.R. Smith, Dislocation structures, interfacing, and magnetism in the $L1_0$—MnGa on η⊥—Mn_3N_2 bilayer, Journal of Vacuum Science & Technology A. 37 (2019) 031102. https://doi.org/10.1116/1.5081960.

[60] H. Yang, A.R. Smith, M. Prikhodko, W.R.L. Lambrecht, Atomic-Scale Spin-Polarized Scanning Tunneling Microscopy Applied to Mn_3N_2 (010), Phys. Rev. Lett. 89 (2002) 226101. https://doi.org/10.1103/PhysRevLett.89.226101.

[61] M. Respaud, J.M. Broto, H. Rakoto, A.R. Fert, L. Thomas, B. Barbara, M. Verelst, E. Snoeck, P. Lecante, A. Mosset, J. Osuna, T.O. Ely, C. Amiens, B. Chaudret, Surface effects on the magnetic properties of ultrafine cobalt particles, Phys. Rev. B. 57 (1998) 2925–2935. https://doi.org/10.1103/PhysRevB.57.2925.

[62] B. Issa, I. Obaidat, B. Albiss, Y. Haik, Magnetic Nanoparticles: Surface Effects and Properties Related to Biomedicine Applications, IJMS. 14 (2013) 21266–21305. https://doi.org/10.3390/ijms141121266.

[63] M.J. Calderón, L. Brey, F. Guinea, Surface electronic structure and magnetic properties of doped manganites, Phys. Rev. B. 60 (1999) 6698–6704. https://doi.org/10.1103/PhysRevB.60.6698.

[64] A. Tebano, A. Orsini, P.G. Medaglia, D. Di Castro, G. Balestrino, B. Freelon, A. Bostwick, Y.J. Chang, G. Gaines, E. Rotenberg, N.L. Saini, Preferential occupation of interface bands in La 2 / 3 Sr 1 / 3 MnO 3 films as seen via angle-resolved photoemission, Phys. Rev. B. 82 (2010) 214407. https://doi.org/10.1103/PhysRevB.82.214407.

[65] D. Nečas, P. Klapetek, Gwyddion: an open-source software for SPM data analysis, Open Physics. 10 (2012). https://doi.org/10.2478/s11534-011-0096-2.

7. Figures

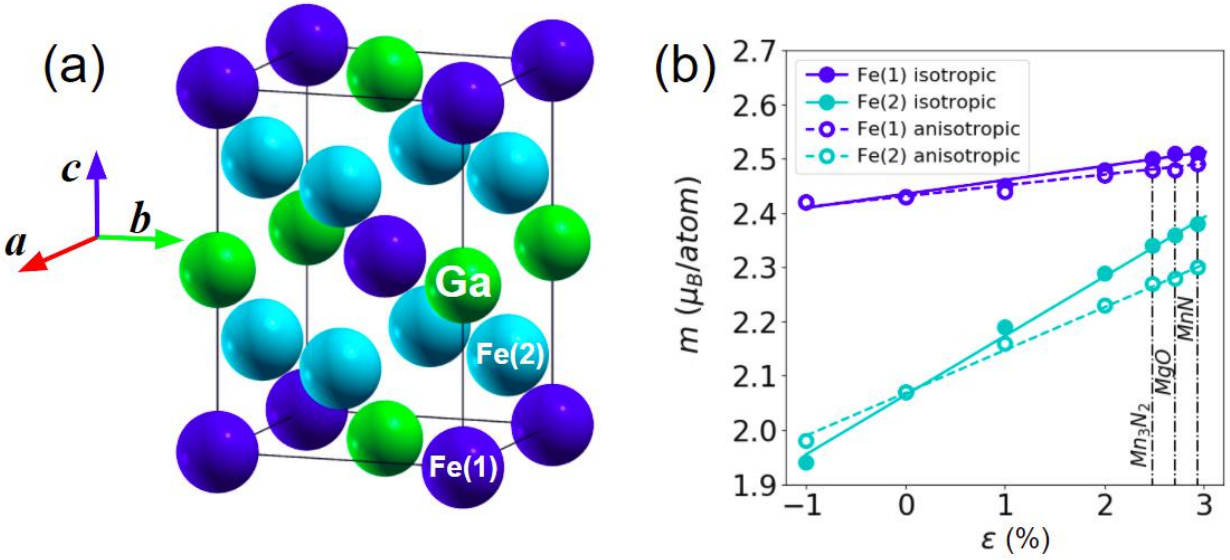

Fig. 1. Results from the bulk structure calculations. (a) Atomic structure of the magnetostrictive $D0_3$-Fe_3Ga alloy. Dark blue, light blue, and green spheres represent the Fe(1), Fe(2) and Ga atoms, respectively. Crystallographic axes are added for the sake of spatial orientation. (b) Fe magnetic moments vs strain plots. Continuous and dashed lines correspond to isotropic and in-plane applied strain, respectively. Perpendicular dot-dash-dot lines indicate the strains applied to $D0_3$-Fe_3Ga by different substrates: 2.48%, 2.71%, and 2.94% for Mn_3N_2, MgO, and MnN, respectively.

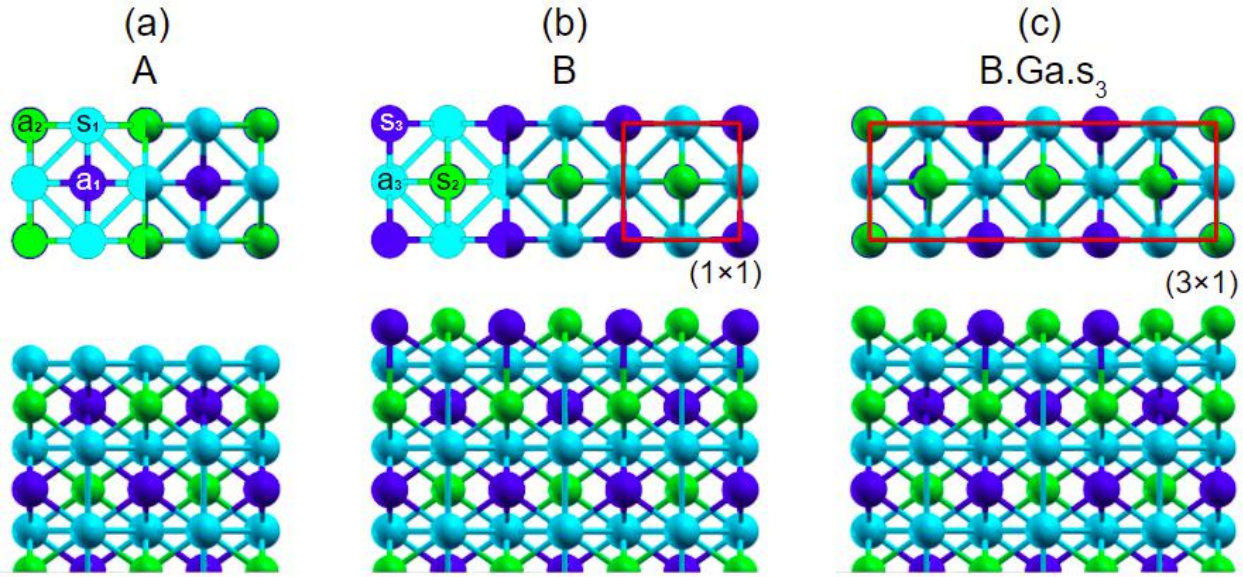

Fig. 2. Top and side views of the proposed surface terminations and the most stable reconstruction. (a) A is an ideal Fe-only terminated (1×1) surface. (b) B is an ideal FeGa-terminated (1×1) surface. Positions a_1, a_2, a_3 stand for adsorption sites and s_1, s_2, s_3 stand for atomic substitutions. (c) Configuration B.Ga.s_3 is a

B surface with a Ga substitution in position s_3. Dark blue, light blue, and green spheres represent the Fe(1), Fe(2) and Ga atoms, respectively.

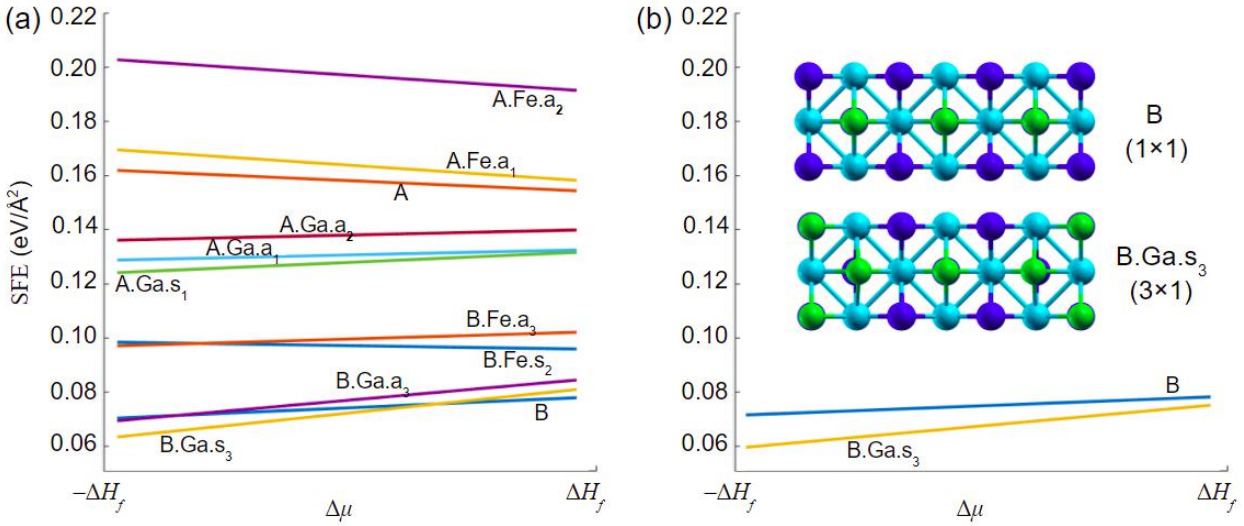

Fig. 3. Surface Formation Energies as defined in Eq. (1) for (a) the proposed $Fe_3Ga(001)$ surfaces, A and B are the ideal non-reconstructed surfaces, respectively (full nomenclature of the models is defined in section 3.2), and (b) effect of the maximum strain on the stability (~3%) for the most stable models (B and B.Ga.s_3).

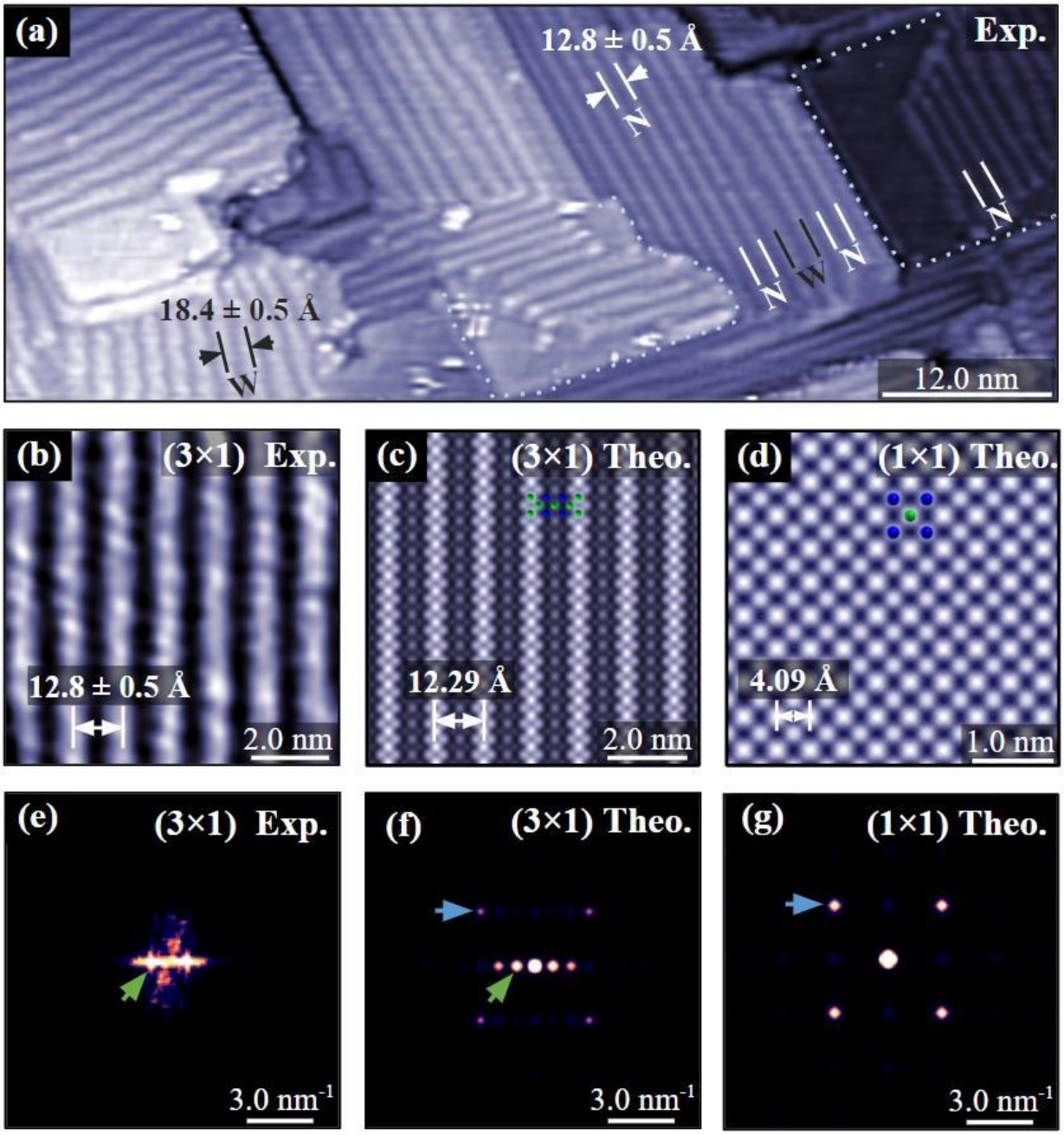

Fig. 4. Experimental and theoretical STM images of the $D0_3$-Fe_3Ga surface. (a) Experimental STM image showing two row-structures, a well-ordered set of narrow rows (3×1) are indicated with a white N and a set of wide rows (4.5×1) are indicated by gray W. Regions without periodic structure are marked by a light blue dotted line. Atomic contrast was enhanced by Laplacian filtering. (b) Zoomed view of the experimental (3×1) row-structure. (c) Tersoff-Hamann-STM image of a (3×1) Ga substituted ideal FeGa termination layer of the Fe_3Ga crystal showing a row-structure in good agreement with the experiment. (c) Tersoff-Hamann-STM image of the ideal (1×1) FeGa termination. (e-g) FFT of the experimental and

theoretical STM images in (b-d) respectively. A dense line of k-points indicates the row-structure (green arrows), while the (1×1) lattice can be seen as a square lattice of k-points (blue arrows).

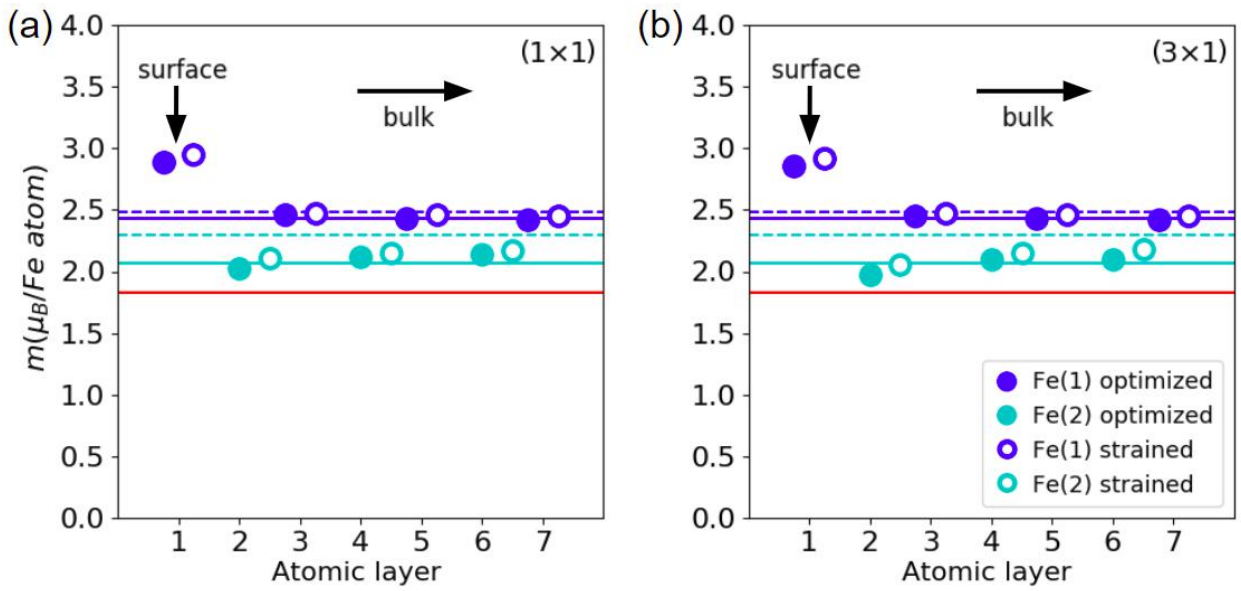

Fig. 5. Analysis of the surface magnetic moments per layer for the non-strained (optimal) and strained (~3%) lattice parameters on the (a) (1×1) and (b) (3×1) reconstructions. Horizontal solid and dashed lines show the values of the magnetic moments from the bulk calculations of Fe(1) and Fe(2), respectively. The red solid line represents the average experimental magnetic moment. Fe(1) and Fe(2) are the same as labeled in Fig. 1.

Atomic description of the row-like domain patterns on $D0_3$-Fe_3Ga.